JOURNAL OF GEOPHYSICAL RESEARCH, VOL. 104, NO. B6, PAGES 13,217–13,233, JUNE 10, 1999

Three-dimensional P and S wave velocity structures of the Coso Geothermal Area, California, from microseismic travel time data

Huatao Wu and Jonathan M. Lees

Department of Geology and Geophysics, Yale University, New Haven, Connecticut

Abstract. High precision P and S wave travel times for 2104 microearthquakes with focus <6 km are used in a non-linear inversion to derive high-resolution three-dimensional compressional and shear velocity structures at the Coso Geothermal Area in eastern California. Block size for the inversion is 0.2 km horizontally and 0.5 km vertically and inversions are investigated in the upper 5 km of the geothermal area. Spatial resolution, calculated by synthetic modeling of a cross model at critical locations, is estimated to be 0.35 km for V_p and 0.5 km for V_s. Model uncertainties are estimated by a jackknife approach and simulation of random and associated picking errors. Low-velocity zones for both P and S waves are identified at geothermal production depths (1–3 km). A large, low V_p (−6%) zone is found at depth 2–2.5 km 2 km southwest of Sugarloaf Mountain where high attenuation has been previously reported. However, a general high-V_p zone is seen under Coso Hot Springs with a slightly low V_s zone, which is characteristic of fluid saturation. The overall distributions of V_p and V_s perturbations do not correlate. An isolated high-V_s (+9%) feature, about 2 km in diameter, is unambiguously seen 2 km due west of Sugarloaf extending from surface to depth. This feature is surrounded by a circular, low-V_s belt of ∼1 km width. The surrounding belt is probably the cracked, high-porosity reservoir/conduit of geothermal fluid flow. In the 2 km southwest Sugarloaf region, we found low V_p and high V_s at geothermal production depths from 1 to 2.5 km. Combined with attenuation results, this may represent a hot, fluid-depleted center of magmatic activity.

1. Introduction

Seismic tomography of travel time data is essential for understanding and modeling of physical processes in the lithosphere [e.g., *Aki et al.*, 1977], tectonically complex areas [e.g, *Walck*, 1988; *Lees and Crosson*, 1989], and geothermal fields [*Zucca et al.*, 1994]. In most cases, compressional wave tomography alone is investigated, chiefly because of the scarcity of good quality S wave arrival data. However, shear velocity is crucial for identifying fluid accumulation and, especially, steam water conditions important in geothermal studies [*Toksöz et al.*, 1976]. Knowledge of shear wave velocity imposes further constraints on the anomalies observed in P wave tomography [*Koch*, 1992]. Shear wave velocity, together with compressional wave velocity, has been used in the past to constrain estimates of the composition and physical state of the continental lithosphere [e.g., *Holbrook et al.*, 1988; *Sanders et al.*, 1988; *Lees and Ukawa*, 1992]. Laboratory experiments on P and S wave propagation provide additional constraints on laterally varying lithological models [*Holbrook et al.*, 1988]. Accurate, three-dimensional P and S wave velocity models at the Coso geothermal field are essential to the understanding of magmatic activity and further development of geothermal energy. Further seismic investigations, like event location and numerical synthetic wave propagation, depend primarily on the accuracy of the available velocity models. Monitoring of geothermal production processes through observation of companion microseismic activity requires precise event locations far exceeding the capability of currently available one-dimensional velocity models [*Lees*, 1998]. In this study we use P and S wave travel time data to derive a detailed, three-dimensional velocity structure through nonlinear, tomographic inversion. Furthermore, we use the three dimensional models to map the extent of magmatic bodies and geothermal temperature variation in the Coso region. This research is made possible by new, high-precision microseismic P and S wave travel time data from a deployment of a 16-station, three-component downhole network operated by the Naval Geothermal Program.

Paper number 1998JB900101.
0148-0227/99/1998JB900101$09.00

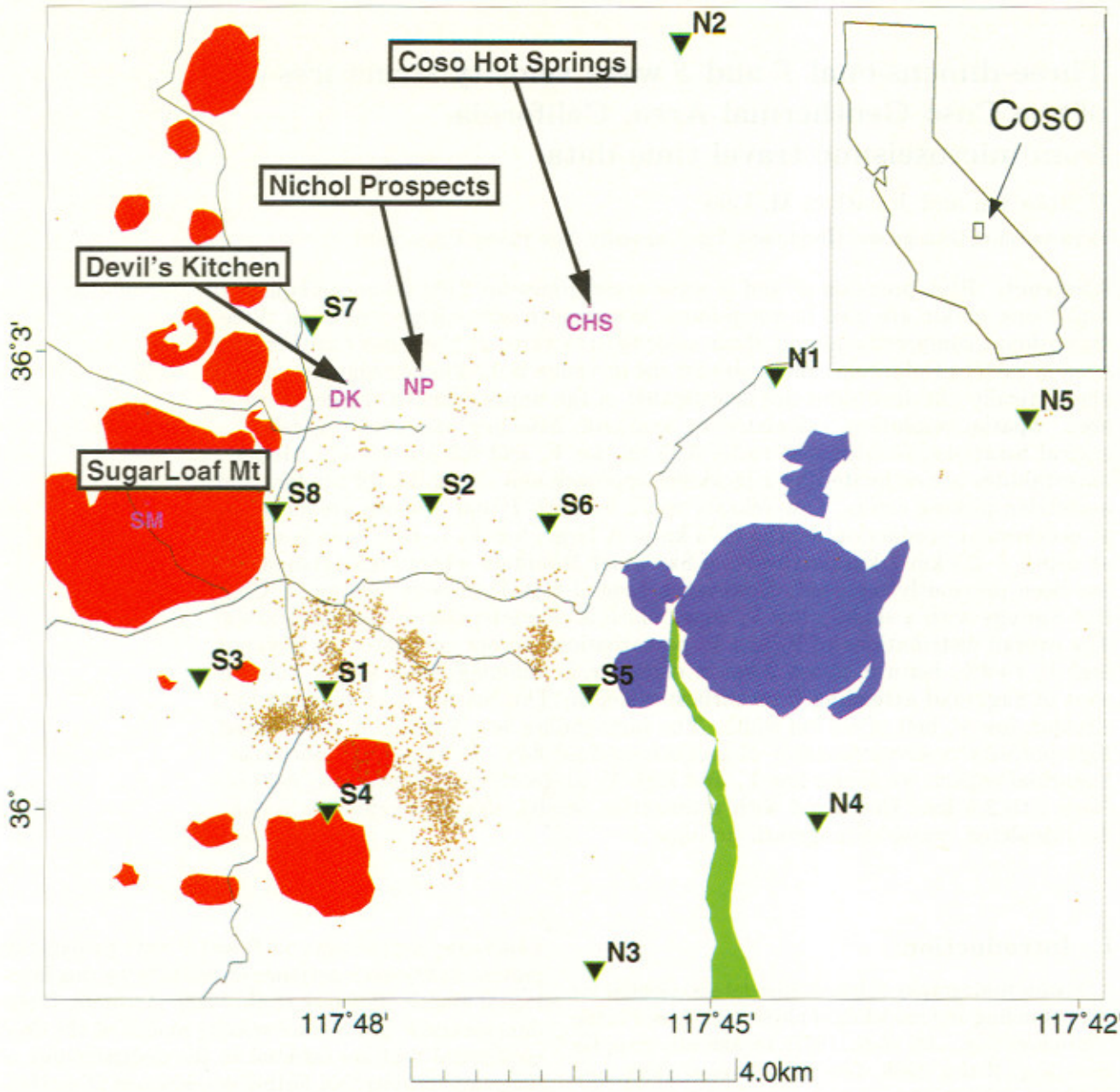

Plate 1. Map view of the geothermal field region at Coso, California. Inset is a California map showing target location. Circular, red features are Quaternary rhyolite domes. Purple regions are areas of thick, Tertiary andesite flows. The green area is a Quaternary basalt flow [*Duffield and Bacon*, 1981]. Dots represent seismic events used in this study, triangles are seismic stations listed in Table 1, and important geographic locations are annotated: DK, Devil's Kitchen; NP, Nicol Prospects; CHS, Coso Hot Springs; SM, Sugarloaf Mountain.

2. Local Geological and Tectonic Setting

The Coso geothermal field (Plate 1) contains the second largest geothermal plant in the continental United States. with an output approximately 300 MW. Tectonically, the Coso region is located between the extensional Basin and Range provinces and dextral strike-slip San Andreas faulting system. To the west is the Coso Range, a horst block immediately east of the Sierra Nevada mountains. Faulting is extensive in the region, including two, nearly perpendicular, sets of normal faults, trending NNE-SSW and WNW-ESE, respectively [*Roquemore*, 1980].

The geothermal field is situated in granitic Mesozoic basement rocks below silicic domes [*Duffield at al.*, 1980; *Duffield and Bacon*, 1981]. The target area (Plate 1) for the tomographic inversion is located in the known

geothermal field. The eastern section (east of station S6) of the target is covered by alluvial deposits, whereas the central north-south trending strip between stations S2 and S8 is about 1–2 km in width and includes exposed Mesozoic basement rock. To the west is the steep Sugarloaf Mountain, the largest rhyolite dome in the region, and Devil's Kitchen (DK), a highly fumarolic area surrounded by rhyolitic tephra. Extensive distributions of intrusions in the last ~4 to 0.04 Myr (Tertiary to Quaternary) have erupted about 35 km^3 of volcanic rocks in the form of rhyolitic domes [*Duffield et al.*, 1980]. The rhyolite magma erupted from a magma chamber that was formed when mantle-derived basalts partially melted crustal rocks. The first geothermal production well producing dry steam was drilled near Devil's Kitchen fumarolic area in 1977. Numerous wells have since been drilled in the area and intensive fractured basement rock is found in many wells [*Combs*, 1980]. The Mesozoic basement is composed principally of granitic and metamorphic rocks, whose composition ranges from granite to gabbro. The intruding rocks, on the other hand, are primarily basalts and rhyolites [*Bacon et al.*, 1980]. Sedimentary rocks only form a thin layer in parts of the region and are relatively unimportant for this study.

Geomorphology at Coso is related to en echelon sets of NNE trending faults and erupted rhyolites along the faults associated with regional NNW right-lateral shearing. These faults do not offset Pleistocene rhyolites, so the rhyolites must have erupted after the last major tectonic movement. Present-day tectonic movements are evidenced by widespread microearthquakes in the region [*Malin*, 1994].

Previous seismic studies of the Coso region using teleseismic travel time residuals identified a low-velocity body in the midcrust (below 5 km) southeast of Devil's Kitchen [*Reasenberg et al.*, 1980], which correlates with a high attenuation anomaly [*Young and Ward*, 1980; *Wu and Lees*, 1996]. A silicic magma body, ~5 km in diameter and 1 km thick, probably partially molten, is predicted under the Coso geothermal field to be at depths >8 km [*Bacon et al.*, 1980]. Previous seismic tomographic studies of P wave velocity variations in a larger region, including Coso, reported no major velocity variations beneath the Coso volcanic field in the upper 5 km [*Walck and Clayton*, 1987]. However, between 5 and 10 km depth, a low-velocity zone of 7% perturbation anomaly was found at the southern end of the Coso geothermal region. Because of the absence of densely sampled high-quality data, these studies failed to provide a high-resolution description of geological features, especially small, shallow (<5 km) structures which directly affect geothermal production.

Recent attenuation and local stress studies reveal structural details related to geothermal activity and associated extraction of fluids from the field [*Wu and Lees*, 1996; *Feng and Lees*, 1998]. Variations of stress at Coso agree well with regional extensional stress, although the southwestern cluster of seismicity appears to have a more horizontal principal stress direction in comparison to other seismic clusters [*Feng and Lees*, 1998]. Attenuation studies revealed a low Q body deep in the central to southwestern part of the field, shoaling to the northeast near Coso Hot Springs (CHS) [*Wu and Lees*, 1996]. The availability of local microseismic data, sampled at 2 ms, enables us to derive a more detailed local velocity structure for this region and to investigate geological correlations.

3. Tomographic Inversion Methodology

Tomographic inversions are formed separately for P and S waves following the standard procedures from the travel time equation. Letting the relative velocity perturbation be $\alpha = (v - v_0)/v_0$, we have

$$T_0 - T \approx \int_{\text{ray path}} \alpha dT \tag{1}$$

where T_0 is the predicted travel time in the reference medium v_0 and T is the measured travel time. The integration is over the ray path calculated in the reference medium v_0. Dividing the target region into rectangular blocks discretizes (1) and produces a system of linear equations $\mathbf{Ax} = \mathbf{b}$. This is solved by the smoothed, least-squares inversion method of *Lees and Crosson* [1989] using

$$\begin{pmatrix} \mathbf{A} \\ \lambda \mathbf{L} \end{pmatrix} \mathbf{x} = \begin{pmatrix} \mathbf{b} \\ 0 \end{pmatrix} \tag{2}$$

where $\mathbf{L}$ is the three-dimensional Laplacian filter and λ is the damping parameter controlling the spatial smoothness of the result. The solution of the (2) is then used to relocate the seismic events. Shifts of hypocentral locations and origin times are used as criteria of convergence, such that when changes are small, iteration is stopped. Events that shift out of the target block are discarded. Modified ray paths and travel time residuals are recomputed by perturbation [*Um and Thurber*, 1987], and a new linear system (2) is again formed and solved. The iteration process stops when the hypocentral shifts are close to the noise level. Both P and S arrivals are used in the relocation procedure. Thus the apparently independent, separate P and S wave inversions are coupled vis-a-vis relocation, albeit slightly.

We divide the target region into 60×60×9 blocks of 0.2 km by 0.2 km horizontally and 0.5 km vertically except the deepest layer, which is 1.5 km thick. Damping parameters are chosen by a trial and error process, and reasonable damping parameters are picked by a subjective balance between residual reduction and smoothness of the resulting image. For P wave inversion, $\lambda_p = 0.5$ was chosen, and for S wave inversion, $\lambda_s = 0.8$. Since $\lambda_s/\lambda_p \approx V_p/V_s$, the dampings on P and S inversions are comparable. Three iterations were carried out before convergence was reached.

4. Data Preparation and Processing

The data used in this study are P and S picks accumulated in a 2-year period between July 1993 and June 1995. The recording system is capable of simultaneously recording 16x3 channels at 2 ms sampling rate. Thus we have at most 16 stations in operation simultaneously. Station locations prior to January 14, 1994, are shown in Table 1 and are plotted in all figures for easy comparison with previous attenuation results of *Wu and Lees* [1996]. The deployment changed twice during the 2-year period, on January 14, 1994 and July 16, 1994. The original data set included 2104 microseismic events in a rectangle bracketed by (35.98°, -117.82°) and (36.09°, -117.70°) (we note that this inversion is smaller in area than the attenuation inversion of *Wu and Lees* [1996]). Choosing those events with hypocentral focus less than 6 km, we obtained 17,758 P picks and 14,959 S picks at 29 physical station locations (Table 2). P wave arrivals are picked universally on vertical components, and S arrivals are picked on either east or north components, depending on which component is clearer. We did not distinguish between S arrival components, although we know that S wave splitting can introduce noise due to this oversight [*Shalev and Luo*, 1995; *Wu and Lees*, 1995]. Anisotropic effects on an isotropic inversion are usually second order to isotropic heterogeneities provided that the ray coverage is sufficient and directionally complete [*Wu and Lees*, 1999]. For the purpose of this study, these second order effects are neglected.

The initial reference velocity model is a one-dimensional velocity model derived by inversion and geological constraints (Table 3) (E. Shalev, personal communication, 1998). In this model, V_s is approximately related to V_p by $V_p \approx 1.705 V_s$, i.e., Poisson's ratio $\sigma \approx 0.236$. Station corrections computed using this model for 29 physical station locations are shown in Table 2. Earthquakes are initially located using this one-dimensional model and origin times are determined to obtain observed travel times. Rays are then traced through this model to compute predicted travel times and travel times for each individual block penetrated. The differences between the predicted and measured travel times, $T_0 - T$, are used in the inversion. The residual distribution before and after inversion were examined closely: distributions of residual misfit after inversion was close to normal distribution. The deviation of P travel time residuals before inversion is 19.3 ms and after inversion is lowered to 15.2 ms, achieving a variance reduction of about 37.8%. The deviation of the original S data is about 59.2 ms and after inversion is 50.8 ms, achieving a variance reduction of about 26.3%. The distributions are both symmetric before and after inversion, indicating the absence of systematic noise. We have visually examined many S picks, compared with predictions, and found that they agree at least statistically very well. We found no evidence of systematic mispicking bias.

Table 1. Station Locations

Station ID	Latitude	Longitude	Elevation km
S1	36°00.7852N	117°48.1522W	1.197
S2	36°02.0210N	117°47.3002W	1.224
S3	36°00.8678N	117°49.1894W	1.178
S4	35°59.9878N	117°48.1359W	1.326
S5	36°00.7686N	117°45.9964W	0.994
S6	36°01.8911N	117°46.3327W	1.108
S7	36°03.1822N	117°48.2752W	1.251
S8	36°01.9631N	117°48.5644W	1.483
N1	36°02.8500N	117°44.4766W	1.128
N2	36°05.0333N	117°45.2600W	1.076
N3	35°58.9500N	117°45.9500W	0.814
N4	35°59.9300N	117°44.1300W	0.731
N5	36°02.5800N	117°42.4200W	1.524

These are stations before January 14, 1994.

The average P travel time is 0.863 s, and the mean S travel time is 1.469 s. The S/P travel time ratio is 1.698, close to, but slightly lower than, the presumed 1.705 from the one-dimensional velocity model ($\sqrt{3}$ is a crustal average for V_p/V_s). This is consistent, in general, with previous field measurements of 1.57 [*Combs and Rostein*, 1976]. An estimate of the average Poisson's ratio, σ, is thus 0.235, nearly the same as the average 0.236 for the one-dimensional model (Table 3). This value is low compared to the generally observed value of 0.25 for the upper crust [*Holbrook et al.*, 1988], and is close to observations for mid-crustal rocks. This may indicate that the petrological conditions at Coso are close to mid-crustal conditions perhaps due to the upwelling of a magma body.

Subjective errors are picked together with P and S arrival picks. The picking errors for P waves are estimated to be ~9 ms and for S waves are ~23 ms. S picks are considerably noisier than P picks due to the fact that the S wave is embedded in the P wave coda. Considering the measured travel time residuals, it is clear that the initial data have signal above the noise level. Care is taken in choosing the proper damping parameter λ to ensure that the residuals after inversion are also above the noise level. We further divide the picking errors by the total travel time and get an estimate of the relative picking errors. The resultant mean relative picking error for P waves is ~1.3% and that for S waves is ~1.8%. These figures are approximately the noise level of the respective data set.

After each iteration, events were relocated using the next iteration three-dimensional P and S velocity models. Differences in event locations after the first iteration are small compared with the total travel time. Origin time shifts are ~30 ms and the hypocenter shifts are around 20–30 meters horizontally and ~100 meters vertically. After the third iteration shifts are practically negligible with origin time shifts ~3 ms and hypocenter shifts ~10 m. We conclude that the non-linear inversion has converged.

Table 2. Physical Station Locations

Station ID	Latitude	Longitude	Elevation km	*P* Correction	*S* Correction
S1(S1)	36°00.7852N	117°48.1522W	1.197	−0.053	−0.062
S2(S2)	36°02.0210N	117°47.3002W	1.224	−0.050	−0.058
S3(S3)	36°00.8678N	117°49.1894W	1.178	−0.046	−0.054
S4(S4)	35°59.9878N	117°48.1359W	1.326	−0.023	−0.026
S5	36°00.4910N	117°45.9070W	1.035	−0.016	−0.008
S6(S6)	36°01.8911N	117°46.3327W	1.108	−0.051	−0.059
S7(S7)	36°03.1822N	117°48.2752W	1.251	−0.024	−0.028
S8	36°03.0850N	117°50.3800W	1.209	−0.006	−0.092
N1(N3)	35°58.9500N	117°45.9500W	0.814	0.068	+0.118
N2	36°01.5363N	117°37.2830W	1.559	−0.025	−0.060
N3	36°08.4820N	117°41.3090W	1.961	−0.002	+0.152
N4	36°02.8500N	117°44.4700W	1.128	+0.065	+0.199
N5(N2)	36°05.0333N	117°45.2600W	1.076	+0.042	+0.073
N6	35°58.9510N	117°48.4865W	1.432	−0.033	+0.046
N7	36°03.8780N	117°59.8000W	1.225	−0.007	−0.045
N8	36°06.9680N	118°00.2440W	1.364	+0.021	+0.205
R3	36°00.8678N	117°49.1894W	1.215	−0.016	−0.025
R5	36°00.4601N	117°45.9964W	1.061	+0.000	+0.000
R6	36°01.8911N	117°46.3327W	1.123	−0.008	−0.008
R8	35°58.9510N	117°48.4865W	1.483	+0.019	+0.040
M2(N4)	35°59.9300N	117°44.1300W	0.731	+0.044	+0.075
M3(N5)	36°02.5800N	117°42.4200W	1.524	−0.051	−0.087
M6	36°00.8678N	117°49.1894W	1.215	+0.000	+0.000
M7	36°02.0210N	117°47.3002W	1.224	+0.000	+0.000
Y1	36°00.4601N	117°45.9964W	1.071	−0.009	−0.071
Y2	35°58.9500N	117°45.9500W	0.561	−0.047	−0.075
Y3	36°01.5360N	117°37.2830W	1.559	−0.016	+0.053
Y4	36°08.5760N	117°41.2890W	1.932	−0.005	+0.076

These renamed station locations are used in inversions. Station names in parentheses are original names in Table 1.

5. Inversion Results of V_p

We discuss our results by first describing the *P* wave anomalies presented in Plates 2 and 3. The quantity shown in the image is percent perturbation of *P* wave velocity $\delta V_p/V_p$. For comparison, the target area plotted in Plates 2 and 3 is the same as in the attenuation study of *Wu and Lees* [1996]. The average percent perturbation for the whole region is about −1.7% and the perturbation ranges from −8% to +3%. We note the asymmetry of positive and negative perturbation ranges. This is chiefly due to the fact that negative perturbations have large amplitude and are limited spatially in the top layers. The top layer, layer 1 (depth 0–0.5 km) is close to the surface where blocks are primarily controlled, in many cases, by nearly vertical rays below a single station. Furthermore, our error analysis suggests these values are highly variable. We therefore do not consider the first layer for interpretation.

Table 3. Depth Profile of Perturbations

Layer	Depth km	V_{p0}	V_{s0}	r_0	V_p	V_s	$\delta V_p/V_p$	$\delta V_s/V_s$
1	0.0 – 0.5	4.50	2.43	1.85	4.50	2.43	+0.02	+0.09
2	0.5 – 1.0	4.51	2.59	1.74	4.48	2.59	−0.58	+0.16
3	1.0 – 1.5	4.92	2.97	1.66	4.86	2.96	−1.27	−0.26
4	1.5 – 2.0	4.92	2.97	1.66	4.80	2.95	−2.39	−0.55
5	2.0 – 2.5	5.46	3.15	1.73	5.25	3.14	−3.81	−0.40
6	2.5 – 3.0	5.46	3.15	1.73	5.21	3.16	−4.62	+0.21
7	3.0 – 3.5	5.54	3.27	1.69	5.42	3.32	−2.34	+1.54
8	3.5 – 4.0	5.54	3.27	1.69	5.51	3.27	−0.50	−0.05
9	4.0 – 5.5	5.58	3.42	1.63	5.58	3.42	−0.01	+0.03

The reference values for the one-dimensional reference model shown in Plate 2 are provided. The rest of the columns are inversion results averaged on each layer. The perturbation values shown in the last two columns are percentage figures, e.g., $100*\delta V_p/V_p$.

Layer 2 (depth 0.5–1.0 km) is near surface so we look for correlations with surface geology. There is a high-velocity zone (HVZ) beneath stations S1 and S4 where volcanic tephra are found at the surface. Another high-velocity zone lies just beyond the eastern edge of Sugarloaf Mountain, between station S3 and Devil's Kitchen. The surface geology at this spot is Mesozoic bedrock, and there is also a nearby cluster of rhyolitic outcrops north of this feature. There are five identifiable low-velocity zones (LVZ) at this depth: (1) close to S3 and the edge of the model; (2) about 0.8 km northeast of station S4; (3) halfway between S1 and S2; (4) 0.4 km southwest of S6; and (5) DK-NP (NP, Nicol Prospects) region. No clear correlation between surface geology and LVZs is apparent.

At depth 1.0–1.5 km (layer 3) the HVZ at Coso Hot Springs becomes a dominant feature. Another prominent HVZ appears in the S1-S3-S4 region, southwest of Sugarloaf Mountain (Plate 2). A high-velocity trend running northeast-southwest from Coso Hot Springs toward S4 corresponds roughly to the central part of the surface Mesozoic bedrock. There is another north-south running high velocity trend from Devil's Kitchen toward S4, subparallel to the previous one. Between these two high-velocity (HV) features, there is a low-velocity (LV) band, also trending north-south, from NP to S1. The trends of these bands are parallel to local faults, suggesting that they may have been formed when magma flow intruded along NNE-SSW trending faults or are somehow otherwise related to these faults. In general, HVZs are well connected, whereas LVZs are scattered throughout the area. The low-velocity feature northeast of S4, seen at shallower depth, expands southwestward and becomes larger.

Layer 4, depth 1.5–2.0 km, is dominated by low velocity features. LVZs are pervasive and well connected. There is a strong low velocity feature ~1 km northeast of station S4. This layer and the next layer (depth 2.0–2.5 km) are the main production depths of the geothermal field. A prominent feature is also the HVZ beneath Coso Hot Springs. In the east, around station S5, there is a HVZ which seems to be the narrowing continuation of a HVZ found at shallower depths. There exists a broad LVZ between S2 and S8 which stretches approximately north-south.

At layer 5 (depth 2.0–2.5) the above mentioned features extend in depth. The three-dimensional variations at this depth are dominated by widespread, large magnitude LVZs with the largest low-velocity anomaly appearing around the S1-S3-S4 region. This is the site and depth of a previously proposed, rising magma channel [*Wu and Lees*, 1996]. It is interesting to note that the HVZ below S5 becomes narrower in layer 5 but is still high amplitude and appears to be dipping to the east. This may well be the site of a fossil magma conduit to the surface. Attenuation results at this site exhibit high Q, suggesting low temperature or low fracture density. We suggest that the high-velocity feature is probably due to less fracture density rather than low temperature [*Wu and Lees*, 1995].

A three-dimensional view of the velocity model can be gained through cross sections (Plate 3). In cross section 1 the HVZ beneath Coso Hot Springs is very clear and is in sharp contrast to a low-velocity body 2 – 3 km depth half way between S8 and Nicol Prospects. In general terms, HVZs are seen in the shallow, northeast blocks, and LVZs are observed in the deep, southwest blocks (Plate 3). In cross section 2, there is a LVZ sandwiched between two HVZs. Traversing these profiles in order from north to south, LVZs first show up in the lower part, broaden southward, and become major features in cross section 3. The deep-rooted HVZ beneath S5 is clearly seen on cross section 3. Figure 1 shows the resultant absolute velocity V_p with a uniform scale for all layers. A low velocity region around S4 and a high velocity region around S5 persistently show up at depth 2–3 km.

It has been assumed that the dominant factor which controls the local velocity structure is heat [*Combs*, 1980]. In a sense, low velocity generally indicates high temperature, and HVZ signals low temperature (Figure 4) [*Christensen*, 1989]. In general terms, the deeper, southwestern part of the target region has higher temperature, while the shallower, northeastern part has lower temperature. The fluid saturation condition as well as crack density could also contribute to the lowering of velocity. Care should be taken when relating LVZs to either hot or fluid-depleted regions. This will be addressed in more detail after presenting the S wave velocity model.

6. Inversion Results for V_s

Next, we describe the S wave travel time inversion (Plates 4 and 5). The S wave result is structurally simpler than the P wave result. The average perturbation is about −0.12% for the target region, and the perturbation ranges from −10% to +9%. The most prominent P wave HVZ beneath Coso Hot Springs (CHS) seen section 5 is not apparent on the S wave inversion, partly due to the ray coverage. The S wave HVZ near CHS does appear in layers 2,3,4 but its amplitude is diminished as compared to the P wave structure. Between S2 and S6, where we located a P wave HVZ, there still exists an unambiguous S wave HVZ. This HVZ feature extends from the surface to the deepest parts of the model. East of station S8 where a high-V_p zone was imaged in the shallower regions, the S waves show a LVZ. This LVZ appears deeper than the high-V_p zone and is separated from the S wave HVZ, between S2 and S6, by a north-south LVZ band west of S2. The LVZ is part of a thick, circular LVZ around the S2-S6 HVZ. The southern leg of this circular zone, which runs east-west, south of the S2-S6 HVZ, is even broader. The east-west trending arc encompasses S5 where we found a deep-rooted HVZ on the V_p inversion. Around sta-

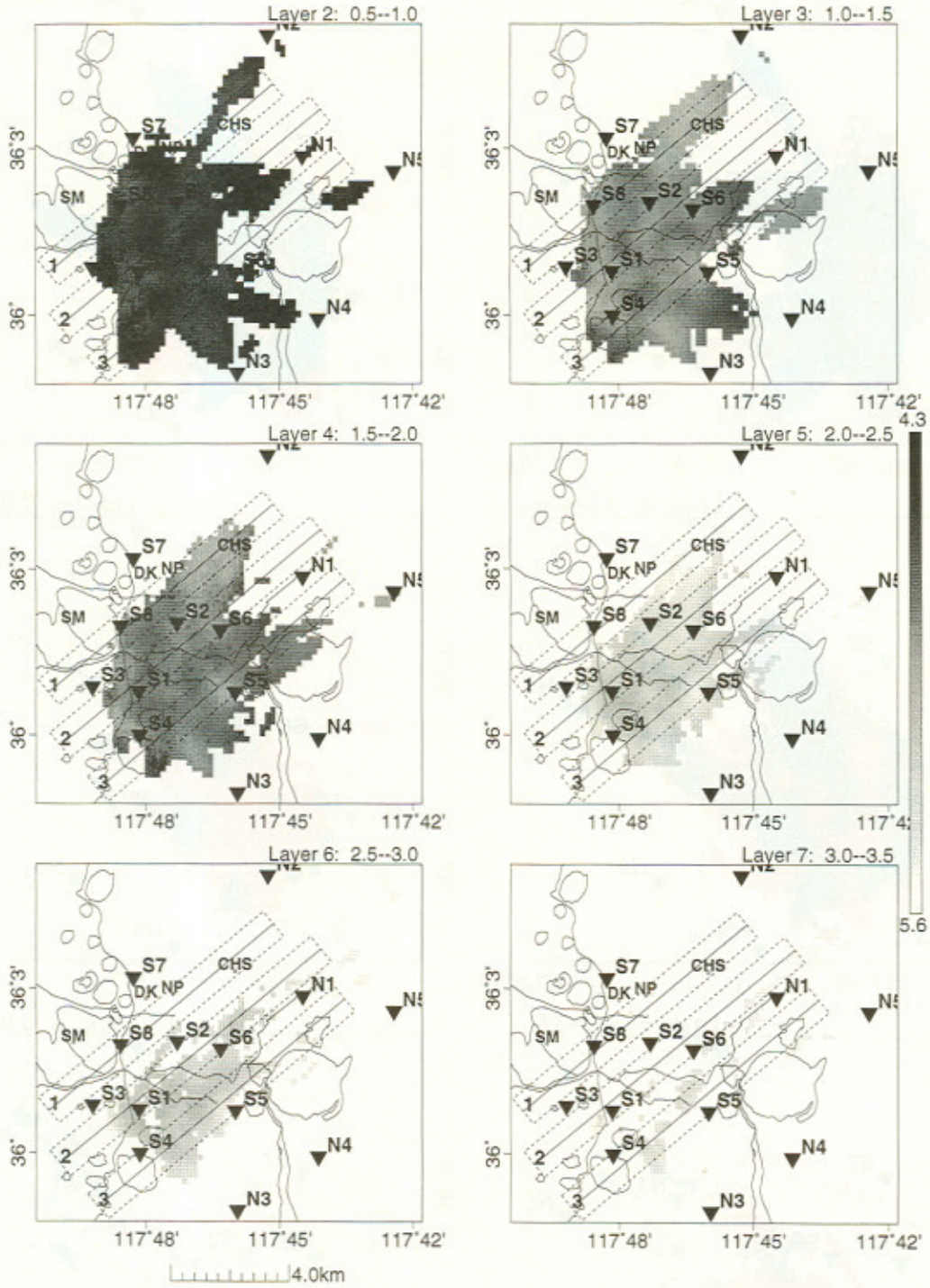

Figure 1. Absolute velocity V_p. The absolute velocities of all layers are plotted in the same scale, and many structural details are suppressed because of the small dynamic range. The low-velocity zone between S1 and S4 and the high-velocity zone around S5 stand out, especially in layers 4 and 5.

tion S1 to the south and north, there is a high velocity region which tapers toward the south at depth (near S1-S3-S4) and shows up as a LVZ in the V_p inversion at depth >1.5 km. There is a strong correspondence to the previously reported low Q feature in this area [*Wu and Lees*, 1996]. The S1-S3-S4 high-V_s feature is more persistent and larger in size than the corresponding low-velocity V_p feature found earlier at the same location and depth. If the rocks in this zone were close to molten, we would not expect such a high S wave velocity. Considering the lowering of V_p, it is also unlikely that it is fluid saturated. We note that there are fewer

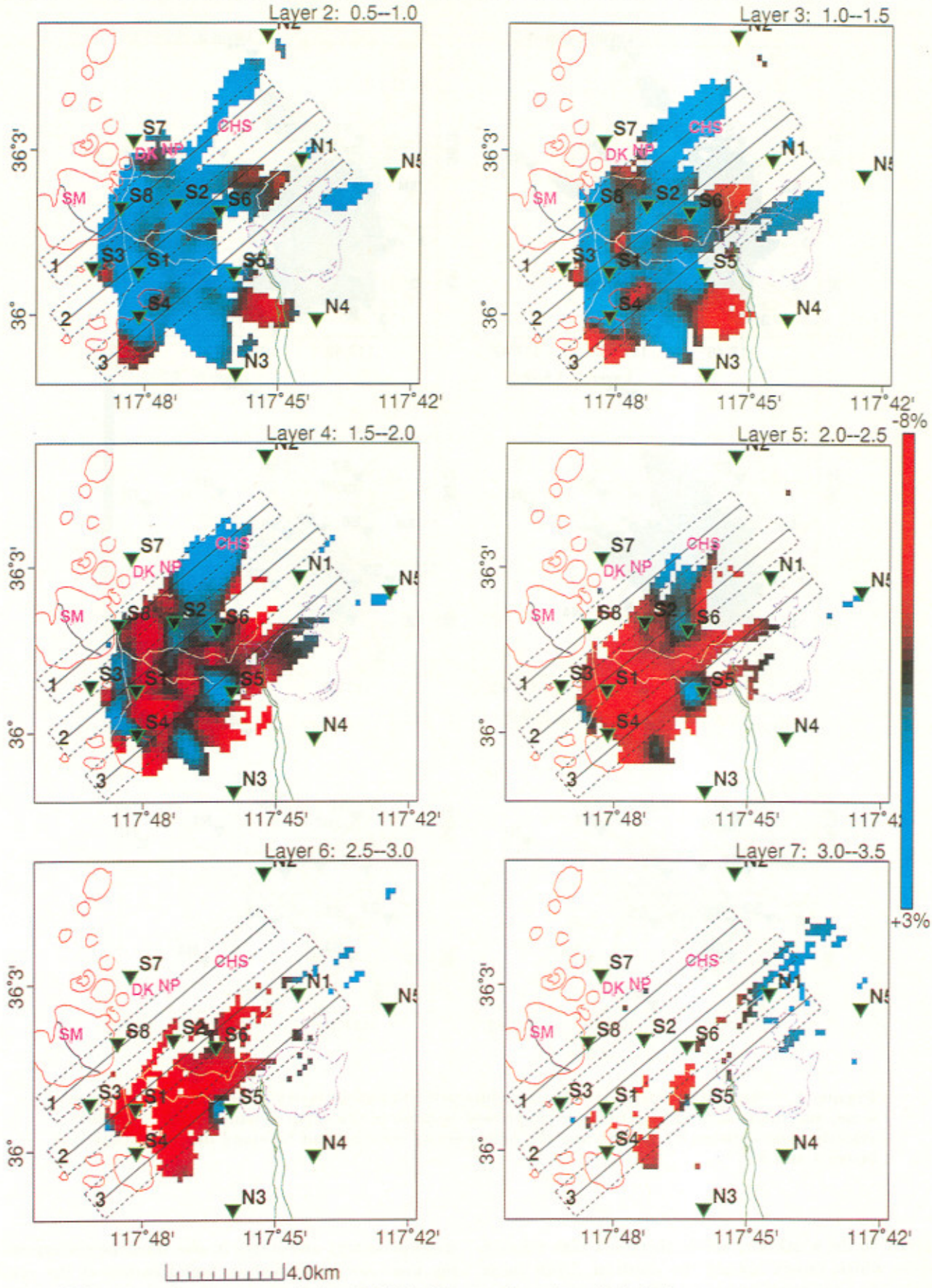

Plate 2. Percent perturbation $\delta V_p/V_p$. The top layer is excluded due to poor ray coverage. Blue areas are positive velocity perturbations representing high-velocity zones (HVZ). Red areas are negative perturbations, or low-velocity zones (LVZ). In general, LVZs are more prominent than HVZs. Hash-marked regions 1, 2, and 3 denote traces of cross sections shown in Figure 2.

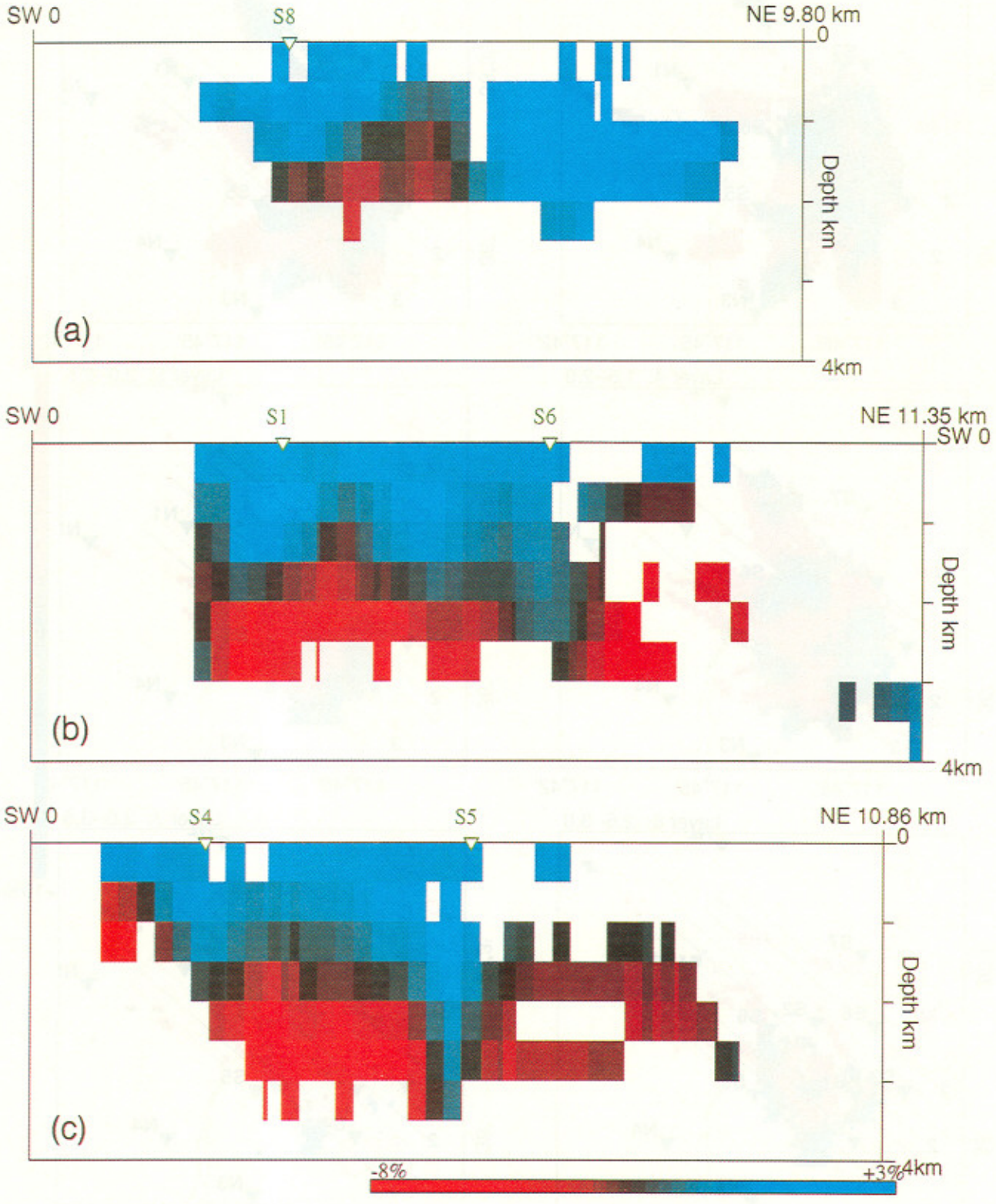

Plate 3. Cross sections of $\delta V_p/V_p$. Traces of the profiles are shown in Plate 5 and the scale of perturbation remains the same. Depth and horizontal axes are drawn to proportion. Cross sections (a) 1, (b) 2, and (c) 3, are as drawn in Plate 2.

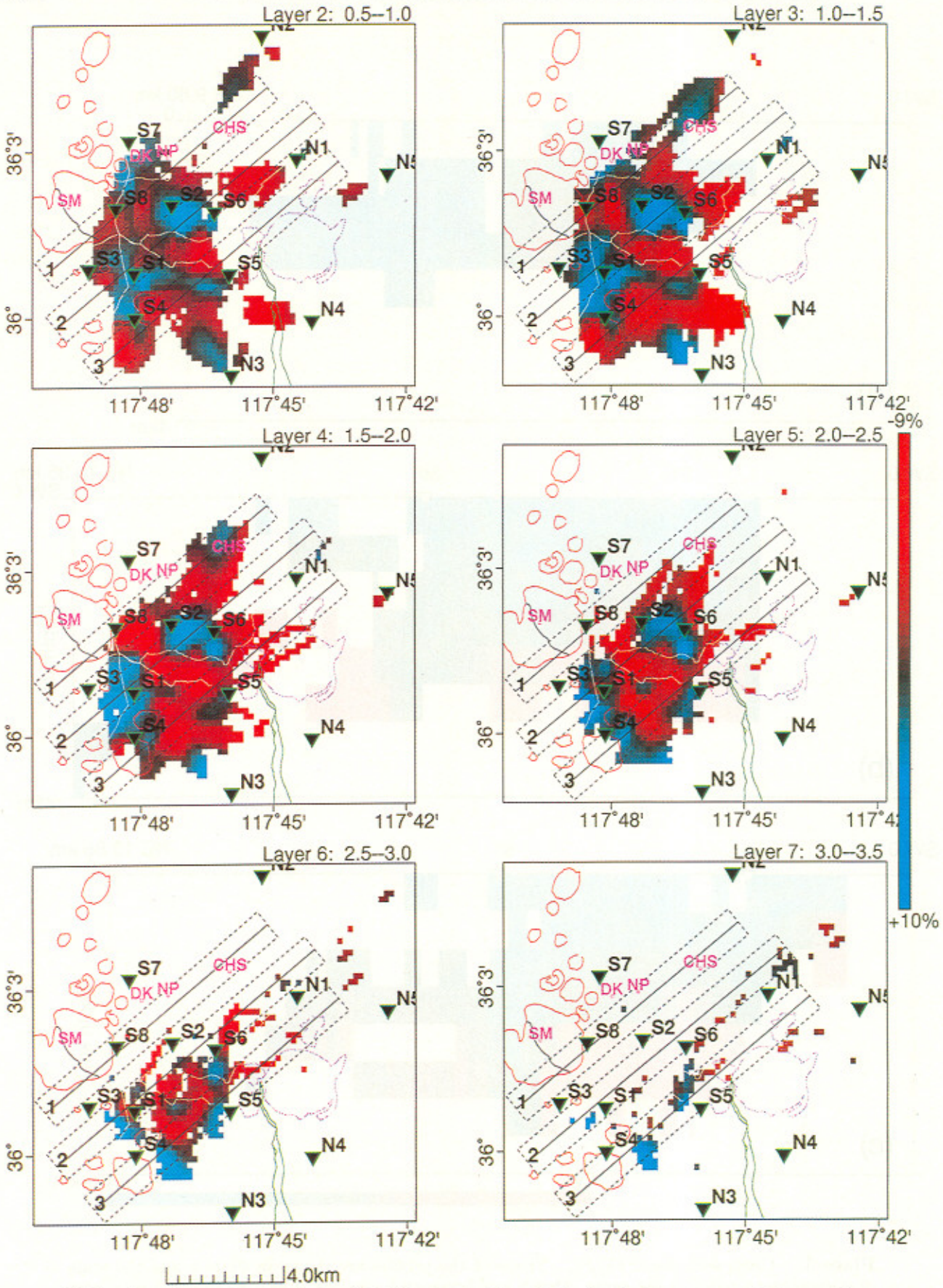

Plate 4. Percent perturbation $\delta V_s/V_s$. As in Plate 2, high-velocity zones are blue and low velocity zones are red. There is a high V_s region between S2 and S6 surrounded by a low-V_s, NW-SE trending belt. High V_p under Coso Hot Springs found in Plate 2 is reversed to slightly low V_s.

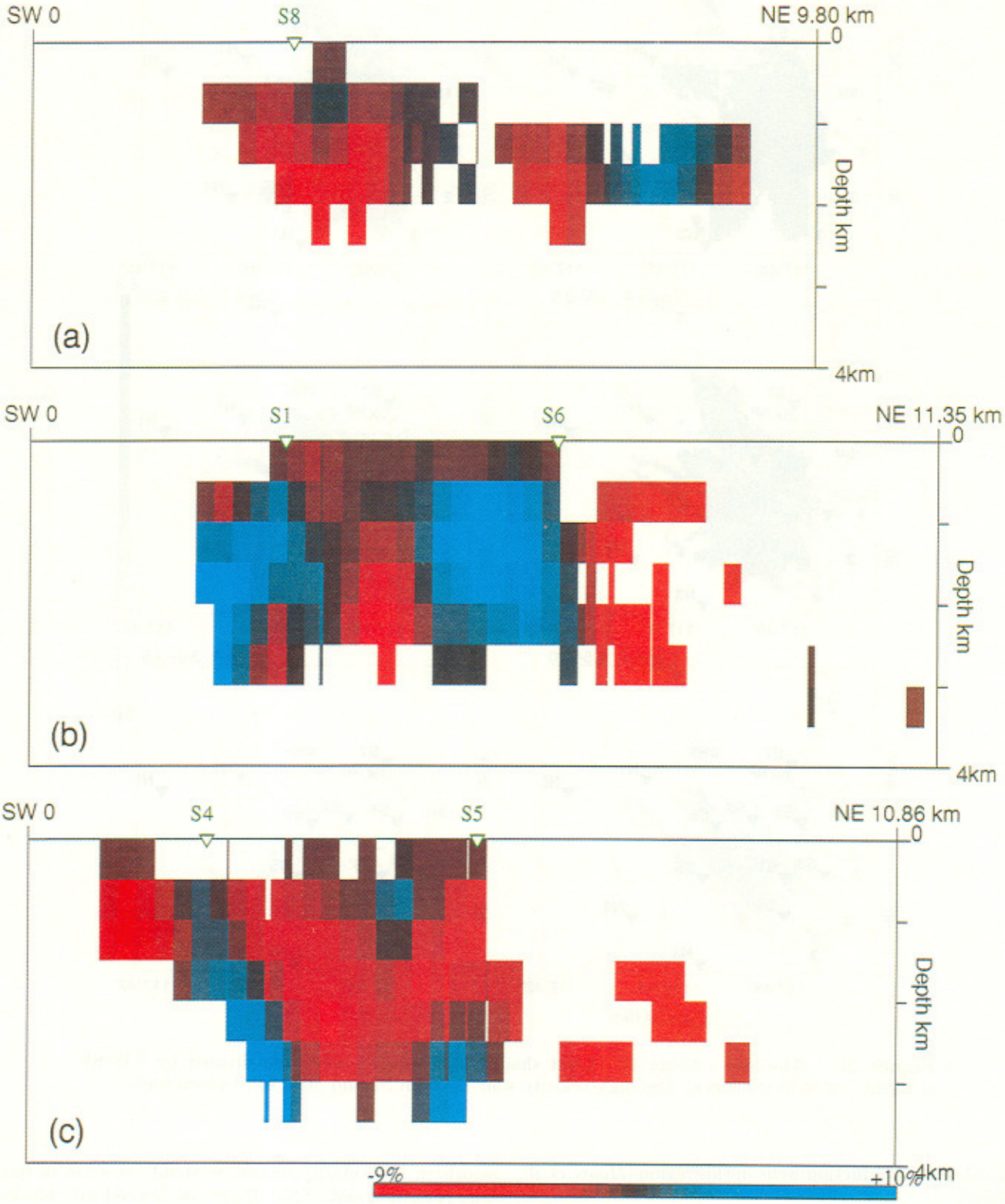

Plate 5. Cross sections of $\delta V_s/V_s$. (a) Cross section 1, as shown in Figure 2. (b) Cross section 2. There are two S wave high-velocity zones below S1 and S6. (c) Cross section 3.

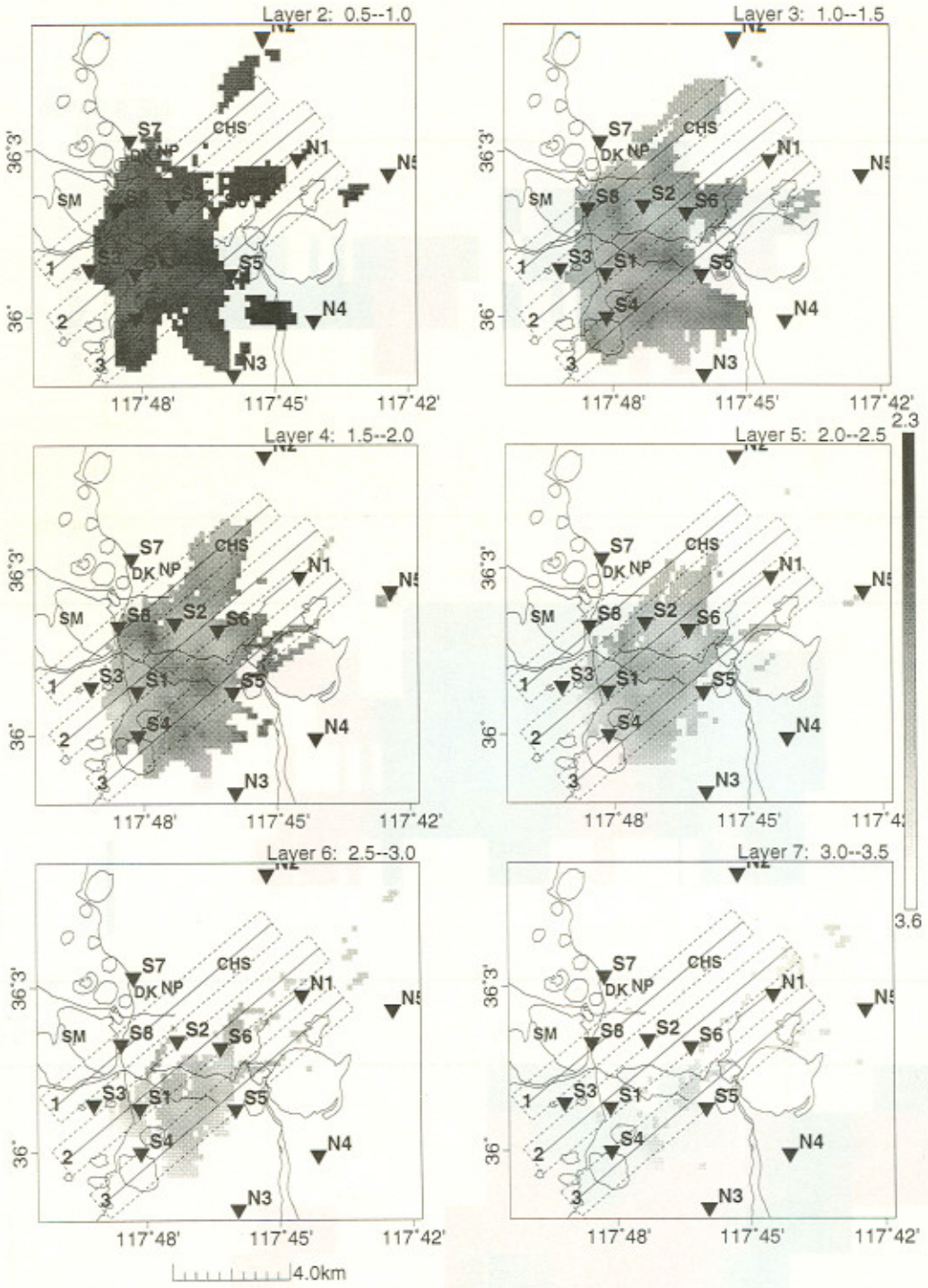

Figure 2. Absolute velocity V_s. Light shaded high-velocity zones are divided by NW-SE trending low-velocity zones. The high-velocity zone between S2 and S6 is most prominent.

geothermal production wells in this region [*Moore et al.*, 1989].

At shallow depth (<2 km), there is a clear, high-velocity demarcation line running from S1 to S5. It divides two wide LVZs north and south of the high-velocity band. This demarcation line diminishes and disappears at depth >2 km. The northern low-velocity block is part of the circular low velocity feature, and the southern low-velocity feature is about ~1.5 km in size and is located east of S4. These two low-velocity blocks connect at depth >2 km. If this demarcation actually exists, it may be the hardened, metamorphic wall of a magmatic intrusion.

Cross sections (Plate 5b) show the bounded wall of low velocity between high-velocity surrounding rocks. This spatially limited feature is as pronounced as in the

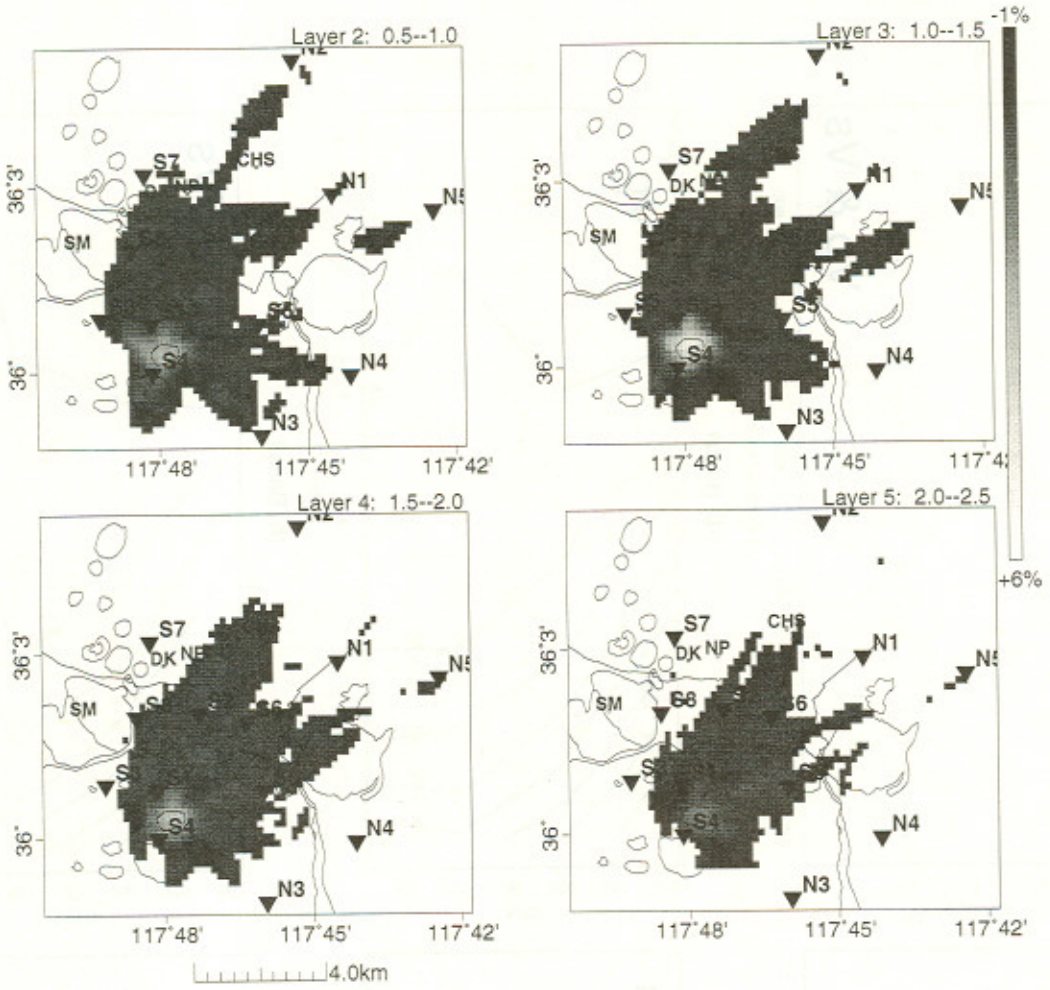

Figure 3. Resolution of a cross in critical regions for P wave ray coverage used in this study. The cross is put horizontally in layer 3 (1–1.5 km) between stations S1 and S4. Each arm of the cross is 0.4 km (2 blocks) wide and 1.2 km (8 blocks) long. The initial perturbation of the cross was 10% spike. The recovered perturbation is 6%.

V_p cross section (Plate 3b) but shallower in depth. The eastern section below S6 shows a strong high velocity and is about 1.5 km in width. It extends across the full depth of the model. Cross section 1 shows uniformly low velocity where we observed a clear demarcation between high and low velocity zones on the corresponding V_p profiles (Plate 3). Cross section 3 also shows overwhelmingly low V_s in contrast to the vertically divided HVZ and LVZ on the V_p image. Figure 2 shows absolute velocity V_s and is useful for relating V_s directly to rock composition through laboratory results. The HVZ around S2 and S6 is clearly evident.

7. Error Analysis of V_p and V_s

The ray coverage of the target is dense in the region we are mainly concerned with, i.e., the S2-S3-S4-S5 area. The jackknife method [*Lees and Crosson*, 1989] is used to estimate V_p and V_s model errors. Error estimates for depths 0.5–3.6 km, based on 100 partitions of the data, are computed. The uncertainties in the perturbation are largest on the north and east edge of the resolved model. The west and south boundaries are resolved very well. The average V_p perturbation error is 0.4%, and the errors spread between 0 and 1%. The average V_s error is 0.8% with the largest error being 1.8%. The errors, in general, are not large enough to change the signs of gross anomalies in the inversion, and the overall velocity structures in the center of the model appear to be consistent.

We tested the resolution power of the specific ray coverage used in this study by generating a synthetic model with a small, horizontal cross at critical areas of interest. The horizontal cross is 2 blocks wide and 8 blocks long in each arm. The inverted V_p image (using the same damping as the real inversion) for a cross close to S4 in layer 3 is shown in Figure 3. The original velocity perturbation was a 10% spike, and the recovered perturbation at the center of the cross is about 5.2%. The cross is resolved unambiguously in layer 3 and is seen smeared in upper and lower layers. The horizontal spread of the inverted cross is about 3~4 blocks in

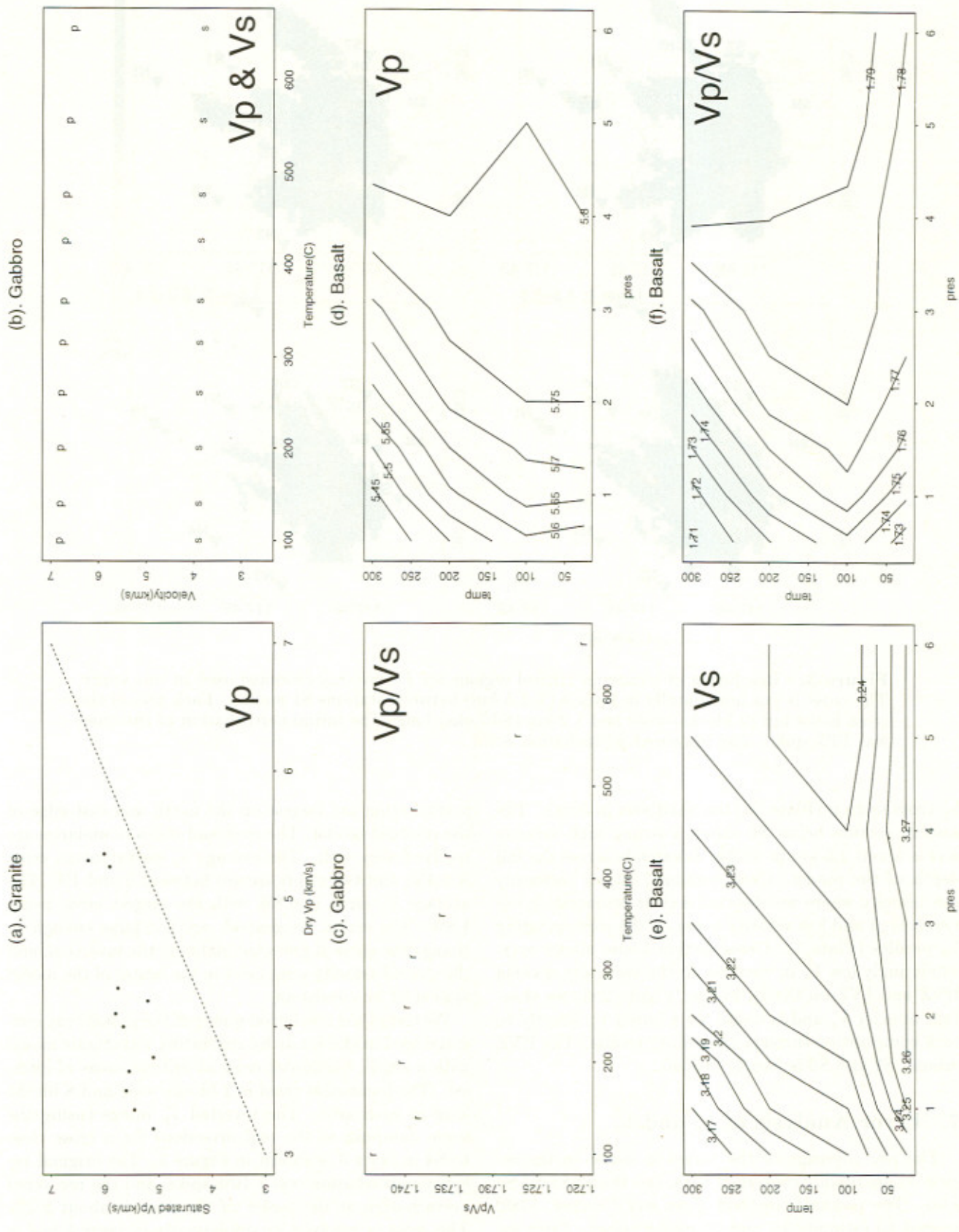
(a). Granite
Vp
Saturated Vp(km/s)
Dry Vp (km/s)
(b). Gabbro
Vp & Vs
Velocity(km/s)
Temperature(C)
(c). Gabbro
Vp/Vs
Vp/Vs
Temperature(C)
(d). Basalt
Vp
temp
pres
(e). Basalt
Vs
temp
pres
(f). Basalt
Vp/Vs
temp
pres

width, giving a resolution roughly 0.35 km. For S wave synthetic tests at the same location, we have recovered an amplitude of 5.0% and slightly larger spatial resolution of 0.5 km (2.5 blocks).

The maximum errors in picking of P arrival times are estimated to be approximately 5 samples (~9 ms) and those for S arrivals are approximately 12 samples (~23 ms). In picking arrivals, analysts often tend to bias arrival time estimates late rather than early, since the onset of the signal is often unclear, obscured by spreading and (in the case of S wave) coda. To investigate the effects of picking errors of this magnitude on the current inversion, two synthetic experiments were examined by assuming different analyst picking behaviors. The effects of the errors are largest when they are all in phase; that is, all errors are of the same sign. The first experiment assumes that all errors have the same bias; that is, all the picks are delayed by the maximum picking error. This is a very extreme case considering that we are using more than 10,000 picks. As expected, results of the experiment are largely controlled by ray coverage. The total variance reduction for associated error perturbed P picks (i.e., all picks are perturbed by the maximum error in the same direction) is 1.3% and that for associated S picks is 14.3%. The resultant P perturbation ranges from -0.5% to +3.0%, and the spread of S perturbation, larger than P, is from -2% to +4%. So if all the errors were correlated and systematic, we would expect these fluctuations in our models. In the second experiment the picking errors are assigned random signs with magnitude of the maximum error bars. This situation better simulates true picking practice. The variance reduction for the random flipping sign case is 1.2% for P waves and 1.1% for S waves. The range of P perturbation noise is, not surprisingly, symmetric from -0.8% to +0.8%, and the range in S is nearly symmetric (-1.0% to +0.9%). This further suggests that systematic error is not present in the data set and station corrections were chosen properly. The actual errors are somewhat between these two extreme cases, and the model error thus introduced falls between these cases. This independent error estimate further confirms the conclusion drawn earlier from the jackknife analysis that errors in our model are not large enough to alter our interpretation of large-scale anomalies.

8. Discussion

Seismic velocity variations depend on many physical conditions, and it is sometimes difficult to isolate specific causes for observed anomalies in three-dimensional inversions. Physical factors such as composition, fractures, cracks, porosity, saturation conditions, and temperature, as well as ambient pressure, all play a role in velocity variations. Of course, composition is a fundamental factor. Generally, igneous rocks exhibit higher velocity than sedimentary rocks, although these results are drawn from laboratory settings for acoustic waves [*Christensen*, 1989]. Considering that seismic waves observed at Coso have wavelength ~500 meters at ~10 Hz, rocks appear relatively uniform at such dimensions. When the composition is uniform, both P and S wave velocities decrease with increasing temperature [*Christensen*, 1989] (Figure 4). However the rate of decrease for P and S waves are different. V_p generally decreases faster, so the ratio V_p/V_s also decreases with increasing temperature (Figure 4) [*Christensen*, 1989]. Randomly fractured media have both smaller V_p and V_s, while V_p decreases slower than V_s, suggesting that V_p/V_s should increase with more fractures [*Schön*, 1996]. Ambient pressure also is a factor for seismic velocity, with V_p, V_s, and V_p/V_s all increasing with pressure (Figure 4) [*Christensen*, 1989]. Finally, fluid saturation generally induces higher velocity for V_p, inducing an increase in V_p/V_s (Figure 4a). In the following, we discuss some of

Figure 4. Laboratory measurements of rock properties for some common igneous rocks under changing physical conditions [after *Christensen*, 1989]. Figures 4a–4c are for granite and gabbro, and Figures 4d–4f are for basalt. (a) Effects of fluid saturation on P wave velocity. Each dot represents a measured granitic sample with varying degrees of saturation. The dashed line represents equal velocity in dry and saturated state. All measurements with saturated rock are above the dashed line. Saturated granite has higher compressional velocity. (b) Effects of temperature on P and S wave velocity of gabbro. Marker "p" indicates a measurement of P velocity, and "s" indicates a measurement of S wave velocity. Hot rocks have definitely lower velocities. (c) Velocity ratio $r = V_p/V_s$ from Figure 4b are plotted. Ratio r, similar to V_p and V_s, decreases in general trend with temperature. The sometime irregular trend is due to experimental errors. (d) Effects of temperature and ambient pressure on V_p of basalt. The isovelocity lines generally trend toward upper right, indicating that rising temperature and rising pressure tend to cancel each other's effects. (e) Effects of temperature and ambient pressure on V_s of basalt. The isovelocity lines again trend upright as in V_p case. However, the slope is quite different from V_p. Temperature seems to have a relatively larger leverage over V_s than ambient pressure. That is, V_s is more sensitive than V_p to temperature changes. (f) Effects of temperature and ambient pressure on the V_p/V_s ratio of basalt. There are two trends of the iso-r lines divided by the temperature of 100°. Iso-r trends upright when temperature >100° while it trends downright when temperature is <100°.

these factors and how they affect our interpretation of the velocity anomalies observed at Coso.

The correlation of absolute velocity to rock composition is not unique. In some restricted circumstances, where only a few alternative rocks are in question, we can use velocities alone to determine lithology [*Tatham*, 1982]. From a lithologic standpoint we expect to see higher velocities in cooled mafic rocks which originate in the upper mantle, and lower velocities in more felsic materials. Surface geology at Coso, however, exhibits both felsic rhyolites and mafic basalts. If we assume there is a deep, mafic intrusion in the southwest portion of the field (S1-S3-S4), our observations of lower P velocity and high attenuation (at depths greater than 2.0 km) indicate the presence of mafic rocks upwelling at very high temperatures, in agreement with heat flow anomalies for this region. Lower-velocity felsic material, alternatively, may also produce the anomalies observed. Since we do not have access to detailed data on lithologic variations at these depths, we can not be definitive in providing a lithologic explanation.

In terms of fractures, on the other hand, low V_p with normal V_s indicates aligned, planar cracks perpendicular to wave propagation directions. Low V_p with low V_s indicates random fracture orientations and high V_p, high V_s suggests the absence of fractures. Normal V_p with low V_s may point to aligned linear cracks, oriented along the wave propagation direction. Lowering of V_p/V_s can correspond to the closing of microcracks under increasing confining pressure [*Nur and Simmons*, 1969]. At Coso the general crack pattern is probably aligned with the local faulting system. However, there are two nearly perpendicular sets of faults in the Coso region, trending NNE and WNW [*Roquemore*, 1980], so a single fracture direction is hard to define. There is some clustering of fault patterns in the Coso region with eastern sections trending WNW and northern sections ENE. The S1-S3-S4 region (>2 km depth) has low V_p and high V_s, and probably has many oriented cracks. In fact, focal mechanism studies have identified this region as having a different stress pattern than the rest of the Coso field [*Feng and Lees*, 1998]. Rays in this region are largely vertical, suggesting that cracks are roughly horizontal. The S2-S6 high S velocity region also has high V_p and is probably a candidate for low crack density. The circular, low-V_s belt around S2-S6 also has slightly lower V_p, indicating high crack density with random orientations. Since randomly oriented cracks can induce high permeability, this belt is possibly a fluid conduit. It is interesting to note that the Coso Hot Springs region has higher V_p and normal V_s. This suggests aligned cracks in the direction of wave propagation. Coincidentally, rays used in this study are mostly NE-SW, under Coso Hot Springs. If this high V_p feature indicates aligned cracks, the cracks should be aligned NE-SW conforming to the local fault direction [*Duffield and Bacon*, 1981]. Further study is needed to prove these conjectures. Another high V_p/low V_s region is found northwest of S5 at all depths. Rays in this region are mostly east-west and the inferred crack direction is similar. This crack direction is, again, almost parallel to the dominant fault direction observed in this part of the target [*Roquemore*, 1980].

Fluid saturation conditions also can affect seismic velocity [*Christensen*, 1989] (Figure 4a). In an experiment with sandstone, saturation increases V_p while decreasing V_s, effectively increasing V_p/V_s ratio and Poisson's ratio [*Ito et al.*, 1979]. Saturated, unconsolidated sediments typically have high V_p/V_s ratio [*Nicholson and Simpson*, 1985]. Saturation conditions can thus be inferred from the comparison of V_p and V_s data. V_p is expected to increase when the saturation of the porous rock increases, while V_s remains nearly constant [*Ito et al.*, 1979]. A few regions with similar characteristics at Coso can be identified. A prominent region showing such characteristics is under Coso Hot Springs. There is a drastic high V_p accompanied by nearly zero $\delta V_s/V_s$ perturbation. The low V_s belt around S2-S6 region may be another possible fluid saturated region with elevated V_p and depressed V_s. A more detailed discussion of V_p/V_s ratio will appear in a forthcoming paper devoted specifically to the relationship of Poisson's ratio $V_p * V_s$ products and porosity estimates.

Attenuation is an independent indicator of temperature and fracture conditions [*Wu and Lees*, 1996]. Low Q indicates either hot or soft rock, while high Q indicates the opposite. The region around S1 at depth 1.5–3 km exhibits high attenuation [*Wu and Lees*, 1996], low V_p, and high V_s. This region may contain soft, hot rock and is fluid depleted. In contrast, at the same depth around S6 we find low attenuation and high velocity, which may point to hard, cold rocks. In the north-south, elongated region east of S8 (eastern edge of Sugarloaf Mountain, width ~1 km), we observe high attenuation, slightly low V_p, and low V_s. This hot, probably randomly cracked region is a potentially saturated, accumulating reservoir of geothermal fluid.

9. Conclusion

Examination of detailed velocity inversion results from microseismic travel time data in the Coso region reveals structural features associated with the geothermal setting: heat, crack distribution and fluid saturation is identified and delineated. Low velocity zones (LVZ) for both P and S wave are identified at geothermal production depths (1–3 km). A large, low V_p (−6%) zone is found at depth 2–2.5 km beneath station S1, where high attenuation was previously reported. However, a large-amplitude high-V_p perturbation zone is seen under Coso Hot Springs accompanied by normal V_s, and this is interpreted as fluid accumulation. The overall distribution of V_p and V_s perturbations do not correlate directly. An isolated high-V_s feature, ~2 km in diameter, is unambiguously seen west of Sugarloaf Mountain, between stations S2 and S6, which extends from the sur-

face to the lower depths of the model. A thick, circular S wave low-velocity zone, ~1 km in width, is found around this high V_s feature. This is interpreted to be a fossil fracture left by magmatic intrusion that has high crack density. It may serve as the main horizontal conduit supplying the Coso region with geothermal fluid.

Acknowledgments. We thank the Navy Geothermal Program for funding this project (awards N68936-94-R-0139 and N68936-97-C-0001) and for providing seismic data. We further acknowledge CalEnergy Co. and Peter Malin (Duke University) for data and valuable comments. Two anonymous reviewers and Associate Editor George Zandt provided helpful comments.

References

Aki, K., A. Christoffersson, and E.S. Husebye, Determination of the three-dimensional seismic structure of lithosphere, *J. Geophys. Res., 82*, 277-296, 1977.

Bacon, C. R., W. A. Duffield, and K. Nakamura, Distribution of Quaternary rhyolite dome of the Coso Range, California: implications for the extent of the geothermal anomaly, *J. Geophys. Res., 85*, 2422-2433, 1980.

Christensen, N. I., Seismic velocities, in *CRC Practical Handbook of Physical Properties of Rocks and Minerals*, edited by R. S. Carmichael, pp. 1-228, CRC Press, Boca Raton, Fla., 1989.

Combs, J., Heat flow in the Coso Geothermal Area, Inyo County, California, *J. Geophys. Res., 85*, 2411-2424, 1980.

Combs, J. and Y. Rostein, Microearthquake studies at the Coso Geothermal Area, China Lake, California, in *Proceedings of the 2nd United Nations Symposium on the Development and Use of Geothermal Resources*, vol. 2, pp. 909-916, U.S. Govt. Print. Off., Washington, D.C., 1976.

Duffield, W. A. and C. R. Bacon, Geologic map of the Coso volcanic field and adjacent areas, Inyo County, California, *U.S. Geol. Surv. Misc. Invest. Ser., MAP-1200*, 1981.

Duffield, W. A., C. R. Bacon, and G. B. Dalrymple, Late Cenozoic volcanism, geochronology and structure of the Coso Range, Inyo County, California, *J. Geophys. Res., 85*, 2381-2404, 1980.

Feng, Q., and J. M. Lees, Microseismicity, stress, and fracture within the Coso Geothermal Field, California, *Tectonophysics, 289*, 221-238, 1998.

Holbrook, W. S., D. Gajewski, A. Krammer and C. Prodehl, An interpretation of wide-angle compressional and shear wave data in southwest Germany: Poisson's ratio and petrological implications, *J. Geophys. Res., 93*, 12,081–12,106, 1988.

Ito, H., J. DeVilbiss, and A. Nur, Compressional and shear waves in saturated rock during water-steam transition, *J. Geophys. Res., 84*, 4731-4735, 1979.

Koch, M., Bootstrap inversion for vertical and lateral variations of the S wave structure and the v_p/v_s-ratio from shallow earthquakes in the Rhinegraben seismic zone, Germany, *Tectonophysics, 210*, 91-115, 1992.

Lees, J. M., Multiplet analysis at Coso Geothermal Field: Delineating hydrothermal patterns, *Bull. Seismol. Soc. Am., 88*(5), 1127-1143, 1998.

Lees, J. M., and R. S. Crosson, Tomographic inversion for three-dimensional velocity structure at Mount St. Helens using earthquake data, *J. Geophys. Res., 94*, 5716-5728, 1989.

Lees, J. M., and M. Ukawa, The south Fossa Magna, Japan, revealed by high resolution P and S wave travel time tomography, *Tectonophysics, 207*, 377-396, 1992.

Malin, P., The seismology of extensional hydrothermal system, *Trans. Geotherm. Resour. Council, 18*, 17-22, 1994.

Moore, J. N., M. C. Adams, B. P. Bishop, and P. Hirtz, A fluid flow model of the Coso geothermal system: Data from production fluids and fluid inclusions, in *Proceedings, Fourth Workshop on Geothermal Reservoir Engineering*, Stanford Univ., pp. 139-144, Stanford, Calif., 1989.

Nicholson, C., and D. W. Simpson, Changes in V_p/V_s with depth: Implication for appropriate velocity models, improved earthquake locations, and material property of the upper mantle, *Bull. Seismol. Soc. Am., 75*, 1105-1124, 1985.

Nur, A., and G. Simmons, Stress-induced velocity anisotropy in rock: An experimental study. *J. Geophys. Res, 74*, 6667-6674, 1969.

Reasenberg, P., W. Ellsworth, and A. Walter, Teleseismic evidence for a low-velocity body under the Coso Geothermal Area, *J. Geophys. Res., 85*, 2471-2483, 1980.

Roquemore, G., Structure, tectonics, and stress of the Coso Range, Inyo County, California, *J. Geophys. Res., 85*, 2434-2440, 1980.

Sanders, C. L. P. Ho, D. Rinn, and H. Kanamori, Anomalous shear wave attenuation in the shallow crust beneath the Coso volcanic region, California, *J. Geophys. Res., 93*, 3321-3338, 1988.

Schön, J.H., *Physical Properties of Rocks: Fundamentals and Principles of Petrophysics*, vol. 18, *Handbook of Geophysical Exploration*, edited by K. Helbig and S. Treitel, Pergamon, Tarrytown, N.Y., 1996.

Shalev, E., and M. Luo, Tomographic inversion for crack-density in Coso, California (abstract), *Eos Trans. AGU, 76*(46), Fall Meet. Suppl., F351, 1995.

Tatham, R.H., V_p/V_s and lithology, *Geophysics, 47*, 3363-344, 1982.

Toksöz M. N., C. H. Cheng, and A. Timur, Velocities of seismic waves in porous rocks, *Geophysics, 41*, 621-645, 1976.

Um, J., and C. H. Thurber, A fast algorithm for two-point seismic ray tracing, *Bull. Seismol. Soc. Am., 77*, 972-986, 1987.

Walck, M. C., Three-dimensional V_p/V_s variations for the Coso region, California, *J. Geophys. Res., 93*, 2047-2052, 1988.

Walck, M. C., and R. W. Clayton, P wave velocity variations in the Coso region, California, derived from local earthquake travel times, *J. Geophys. Res., 92*, 393-405, 1987.

Wu, H., and J. M. Lees, Anisotropy structure and crack distribution of Coso geothermal area, California, from P wave travel times(abstract), *Eos Trans. AGU, 76*(46), Fall Meet. Suppl., F351, 1995.

Wu, H., and J. M. Lees, Attenuation structure of Coso Geothermal Area, California, from P wave pulse widths, *Bull. Seismol. Soc. Am., 86*, 1574-1590, 1996.

Wu, H., and J. M. Lees, Cartesian parameterization of anisotropic traveltime tomography, in press *Geophys. J. Int.*, 1999.

Young, C. Y., and R. W. Ward, Three-dimensional Q^{-1} model of the Coso Hot Springs known geothermal resource area, *J. Geophys. Res., 85*, 2459-2470, 1980.

Zucca, J. J., L. J. Hutchings, and P. W. Kasameyer, Seismic velocity and attenuation structure of the Geysers Geothermal Field, California, *Geothermics, 23*, 111-126, 1994.

J. M. Lees and H. Wu, Department of Geology and Geophys, Yale University, New Haven, CT 06510. (e-mail: lees@love.geology.yale.edu)

(Received August 1, 1997; revised November 16, 1998; accepted November 23, 1998.)